Characteristic quantum phase in Heisenberg antiferromagnetic chain with exchange and single-ion anisotropies

Yan-Wei Dai,[1,2,*] Xi-Jing Liu,[1,3] Sheng-Hao Li,[1,4] and Ai-Min Chen[5]

[1]*Centre for Modern Physics and Department of Physics, Chongqing University, Chongqing 400044, The People's Republic of China*

[2]*State Key Laboratory of Optoelectronic Material and Technologies, School of Physics, Sun Yat-sen University, Guangzhou 510275, The People's Republic of China*

[3]*The School of Materials Science and Engineering, Chongqing Jiaotong University, Chongqing 400044, The People's Republic of China*

[4]*School of Big Data and Internet of Things, Chongqing Vocational Institute of Engineering, Chongqing 402260, The People's Republic of China*

[5]*School of Science, Xi'an Polytechnic University, Xi'an 710048, The People's Republic of China*

(Received 31 May 2022; revised 2 September 2022; accepted 11 October 2022; published 2 November 2022)

We investigate the ground-state phase diagram for a spin-one quantum Heisenberg antiferromagnetic chain with exchange and single-ion anisotropies in an external magnetic field by using the infinite time-evolving block decimation algorithm to compute the ground-state fidelity per lattice site. We detect all phase boundaries *solely* by computing the ground-state fidelity per lattice site, with the prescription that a phase transition point is attributed to a pinch point on the ground-state fidelity surface. Furthermore, the results indicate that a magnetization plateau corresponds to a fidelity plateau on the ground-state fidelity surface, thus offering an alternative route for investigating the magnetization processes of quantum many-body spin systems. We characterize all phases by using the local-order parameter, the spin correlation, the momentum distribution of the spin correlation structure factor, and mutual information as a function of the lattice distance. The commensurate and incommensurate phases are distinguished by the mutual information. In addition, the central charges at criticalities are identified by performing a finite-entanglement scaling analysis. The results show that all phase transitions between spin liquids and magnetization plateaus belong to the Pokrovsky-Talapov universality class.

DOI: 10.1103/PhysRevE.106.054104

I. INTRODUCTION

In recent years, significant attention has focused on spin-one anisotropic Heisenberg antiferromagnetic chains with exchange and single-ion anisotropies in an external magnetic field [1–9], in part because of the prospect for a feasible experimental realization [10]. The system offers a rich ground-state phase diagram that stems from the competition between different control parameters favoring distinct orderings, which has led to the discovery of a supersolid (SS) phase induced by an external magnetic field [2,3], the salient feature of which is the coexistence of diagonal and off-diagonal order [1]. The system involves competing parameters such as the exchange anisotropy Δ, the single-ion anisotropy D, and the external magnetic field B. As demonstrated in Refs. [4–6], diverse phases such as antiferromagnetic (AFM), ferromagnetic (FM), spin-liquid (SL), large-D, and supersolid (SS) phases occur when the single-ion anisotropy and the external magnetic field are varied for a proper chosen (fixed) value of the exchange anisotropy.

To mention the diversity of the phase in the system, numerical methods, such as the exact diagonalization [6], the effective model and Monte Carlo simulations [2,3], and the density matrix renormalization group (DMRG) in either periodic [1] or open [4] boundary conditions, provide proper probes to explore different aspects of rich behaviors of quantum criticalities underlying the system. Due to the novel physical phenomena in the system, it is challenging to study thoroughly, for example, (i) the existence of a magnetization plateau in the AFM phase, the FM phase, and the 10 phase; (ii) discrimination of commensurate and incommensurate phases; (iii) exploration of the SS phase; and (iv) characterization of the Pokrovsky-Talapov (PT) [11] phase transition lines in the phase diagram. Recently, Zhou *et al.* [12–17] proposed that the ground-state fidelity per lattice site approach in the context of tensor networks is able to be a universal phase transition marker to capture quantum phase transitions [18,19], regardless of whether or not a local order is present. Such a system offers an excellent test bed for a novel fidelity approach to quantum phase transitions. Therefor, it is worthwhile to use the fidelity approach to excavate the phase information in the deeper physics of this complex system.

In this contribution, we investigate the ground-state phase diagram for a spin-one quantum Heisenberg antiferromagnetic chain with exchange and single-ion anisotropies in an external magnetic field with $\Delta = 6$ by exploiting the infinite time-evolving block decimation (iTEBD) algorithm [20]. The iTEBD algorithm does not suffer from any finite-size effect, due to the fact that the translational invariance of the system is exploited to avoid any necessity to perform extrapolations. The ground-state fidelity per lattice site is used to detect all

*daiyw@cqu.edu.cn

the phase boundary lines. All of the phases are also characterized. It is found that a magnetization plateau corresponds to a fidelity plateau on the ground-state fidelity surface, thus offering an alternative route towards the investigation of the magnetization processes of quantum many-body spin systems. Our results show that the mutual information can be used to distinguish the commensurate and incommensurate phases. In addition, from the fidelity platform and the center charge $c = 1$, we verify that all the phase transitions between the SL phases and the magnetization plateau phases belong to the PT universality class.

This paper is organized as follows. Section II briefly describes the spin-one quantum Heisenberg antiferromagnetic chain with exchange and single-ion anisotropies in an external magnetic field. Section III presents the ground-state fidelity phase diagram with the exchange anisotropy $\Delta = 6$. This is achieved by computing the ground-state fidelity per lattice site to identify all the phase boundary lines with pinch points on the fidelity surfaces. The results of the study show that the ground-state fidelity can distinguish all phase transition points. Even for a very narrow exotic SS phase, the singularity remains clearly visible in the ground-state fidelity per lattice site. Section IV presents a finite-entanglement scaling analysis, which allows us to determine both the commensurate $\mathrm{SL(SL_C)}$ and incommensurate $\mathrm{SL(SL_{IC})}$ phases as Luttinger liquids. As such, all phase transitions between the magnetization plateaus and the SLs belong to the PT universality classes [6,11]. Section V characterizes all relevant phases and finds that a fidelity plateau on the fidelity surface corresponds to a magnetization plateau. Finally, Sec. VI is devoted to a summary.

II. MODEL

The spin-one Heisenberg chain with exchange and single-ion anisotropies subject to an external magnetic field is described in terms of the Hamiltonian H:

$$H = \sum_i \left[J\left(S_i^x S_{i+1}^x + S_i^y S_{i+1}^y + \Delta S_i^z S_{i+1}^z\right) + D\left(S_i^z\right)^2 - B S_i^z \right], \tag{1}$$

where i denotes the lattice site; Δ and D are the exchange and single-ion anisotropy, respectively; and B is an external magnetic field applied along the z direction. Generically, one can argue that a negative large D favors the spin components $S_z = 1$ and $S_z = -1$, projecting out the spin component $S_z = 0$, while a positive large D favors the spin component $S_z = 0$. The effect of the external magnetic field B competes with the exchange anisotropy Δ, such that the net magnetization m_z increases with increasing B. Indeed, for a sufficiently large B, the system becomes a fully polarized state. Due to the competition of these interactions, this model has a rich ground-state phase diagram. Here, we fix $J = 1$ as the energy scale and assume $\Delta = 6$. Compared with the result from the DMRG calculation for $\Delta = 5$ [5], the system is induced to a direct phase transition occurs from the SS phase to the 10 phase, as well as from the AFM phase to the $\mathrm{SL_{IC}}$ phase on the ground-state phase diagram for $\Delta = 6$. The SS phase broadens and the $\mathrm{SL_C}$ phase disappears between the AFM phase and the $\mathrm{SL_{IC}}$ phase with increasing the exchange anisotropy Δ.

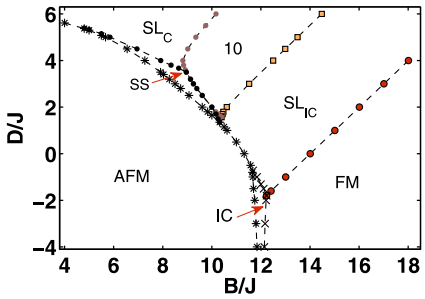

FIG. 1. The ground-state fidelity phase diagram for the spin-1 anisotropic Heisenberg chain in the $(D/J, B/J)$ plane with $\Delta = 6$. Here, we have assumed J to be 1 as the energy scale. The dashed lines are just a guide for the eyes.

Note that in order to check the fidelity per lattice site feasibility, following Ref. [5], the ground-state phase diagram for $\Delta = 5$ is obtained by using the fidelity per lattice site (see Appendix A for details). The overall phase landscape identified from the ground-state fidelity surfaces is consistent with the previous results from DMRG calculations [5].

III. GROUND-STATE FIDELITY PHASE DIAGRAM

Generically, fidelity is a measure of the similarity between two quantum states. A remarkable observation is that the ground-state fidelity $F(B_1/J, B_2/J)$, between the two ground states $|\varphi(B_1/J)\rangle$ and $|\varphi(B_2/J)\rangle$ (with B_1/J and B_2/J being two different values of a control parameter B/J), which is defined as $F(B_1/J, B_2/J) = |\langle\varphi(B_1/J)|\varphi(B_2/J)\rangle|$ mathematically, offers a universal marker in signaling quantum phase transitions in a quantum many-body system. Asymptotically, $F(B_1/J, B_2/J)$ scales as $d(B_1/J, B_2/J)^N$, with N being the number of the sites and $d(B_1/J, B_2/J)$ being the averaged fidelity per lattice site [13]. In the thermodynamic limit, the ground-state fidelity per lattice site $d(B_1/J, B_2/J)$ [13] is defined as

$$\ln d(B_1/J, B_2/J) \equiv \lim_{N\to\infty} \frac{\ln F(B_1/J, B_2/J)}{N}. \tag{2}$$

As argued in Refs. [12–16], this fundamental quantity captures quantum criticality underlying quantum many-body systems in condensed-matter physics, with the prescription that a phase transition point is attributed to a pinch point occurring on the ground-state fidelity surface. In passing, we mention that a pinch point is defined as an intersection point of two perpendicular singular straight lines.

To determine the ground-state phase diagram, we use the iTEBD algorithm, which represents ground-state wave functions in terms of the infinite matrix product state (iMPS) forms [20]. The algorithm provides an efficient means to compute the ground-state fidelity for one-dimensional quantum many-body lattice systems. This enables us to determine the ground-state phase diagram with no prior knowledge of the order parameters.

Figure 1 plots the ground-state fidelity phase diagram in the $(D/J, B/J)$ plane. It consists of the conventional AFM and FM phases, an exotic SS phase, the $\mathrm{SL_C}$ phase, and the $\mathrm{SL_{IC}}$ phase, as well as the 10 phase and the incommensurate (IC) phase with exponentially decaying transversal spin correlations [21].

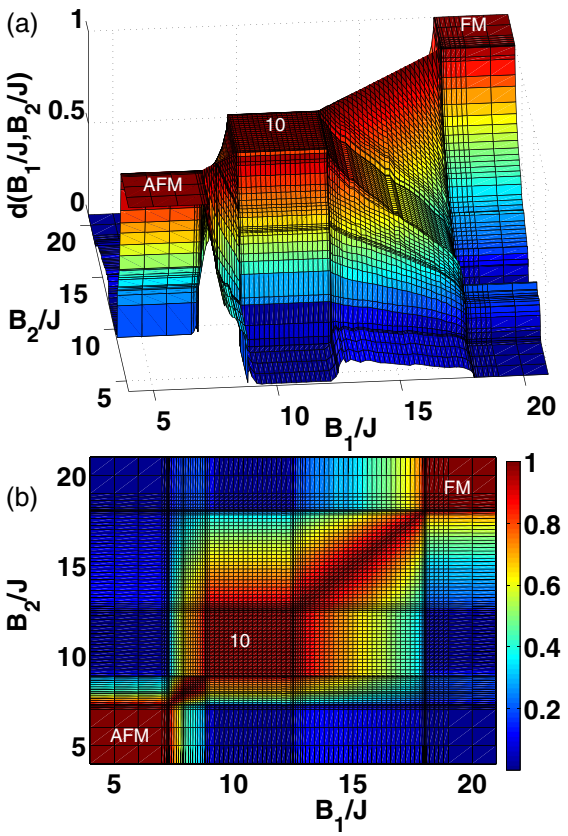

FIG. 2. (a) The ground-state fidelity surface defined by the ground-state fidelity per site $d(B_1/J, B_2/J)$ as a function of B_1/J and B_2/J, two different values of the external magnetic field strength B/J. (b) The contour plot of $d(B_1/J, B_2/J)$, containing AFM, SS, and FM phases. Here, we have chosen the single-ion anisotropy D to be equal to 4 as a typical example to compute the ground-state fidelity per lattice site.

The dash lines are just a guide for the eyes, and the phases are characterized in detail in Sec. V. Note that the 10 phase is a magnetization plateau with an alternative arrangement of the spin components $S^z = 1$ and $S^z = 0$ [3], with the magnetization $\langle (S_i^z + S_{i+1}^z)/2 \rangle = 0.5$. Here, we have taken the bond dimension χ to be 60. All phase boundary lines are detected from the ground-state fidelity per lattice site. The results offer another example highlighting the connection between critical points for a quantum many-body system undergoing a quantum phase transition and pinch points on a fidelity surface.

To explain how this has been done, we compute the ground-state fidelity per lattice site as a function of B_1/J and B_2/J for a typical (fixed) value of D/J, with B_1/J and B_2/J being two different values of B/J with the bond dimension $\chi = 60$. Figure 2(a) plots the simulation results for the ground-state fidelity per site $d(B_1/J, B_2/J)$, with $D/J = 4$. Five pinch points occur on the ground-state fidelity surface corresponding to the phase transition points. The five phase transition points $B_c(\chi)/J$ are located at $B_c(\chi)/J = 7.27, 7.91, 8.82, 12.49$, and 18.01 between AFM and SS phases, SS and SL_C phases, SL_C and 10 phases, 10 and SL_{IC} phases, and SL_{IC} and FM phases, respectively.

A remarkable feature appears on the fidelity surface in Fig. 2(b). That is, three fidelity plateaus occur, meaning that one single ground-state wave function, which does not depend on the control parameters, describes the entire phase. This is expected because the external magnetic field term $B\sum S_i^z$ is conserved. Thus, the fidelity plateaus arise from level crossings that are due to variations in the external magnetic field strength B/J. Conversely, as clarified in the next section, a fidelity plateau on the ground-state fidelity surface implies a magnetization plateau, which is predicted in Ref. [22].

IV. CENTRAL CHARGE

The von Neumann entropy quantifies the bipartite entanglement in a quantum state. Its behavior at criticality is universal [23]. In our setting, the entire chain is partitioned into two semi-infinite chains. The von Neumann entropy for a semi-infinite chain is defined as

$$S = -\sum_i \Lambda_i \log_2 \Lambda_i, \tag{3}$$

where Λ_i are the eigenvalues of the reduced density matrix and represent the entanglement between two semi-infinite chains. At a critical point, the conformal invariance implies a logarithmic scaling relation of the von Neumann entropy with respect to the bond dimension χ [24–26]:

$$S \sim \frac{c\kappa}{6} \log_2 \chi, \tag{4}$$

where c is the central charge and κ is a finite entanglement scaling exponent. The scaling relation between the correlation length ξ and the bond dimension χ [25] takes the form

$$\xi \sim a\chi^{\kappa}. \tag{5}$$

Equations (4) and (5) constitute the so-called finite-entanglement scaling [24–26], which is reminiscent of the finite-size scaling [27]. In the iMPS representation, for a given bond dimension χ, the correlation length is defined as $\xi(\chi) = 1/\log_2(|\frac{\epsilon_0}{\epsilon_1}|)$, where ϵ_0 and ϵ_1 denote the largest and the second largest eigenvalues of the transfer matrix T [28], respectively. Figure 3 plots the von Neumann entropy $S(\chi)$ and the correlation length $\xi(\chi)$ with the bond dimension χ ranging from 20 to 150 for four chosen points deep inside the SL_C and SL_{IC} phases, respectively. The fitting functions are $S(\chi) = \frac{c\kappa}{6} \log_2 \chi + b$ and $\xi(\chi) = a\chi^{\kappa}$, respectively. The fitting results are listed in Table I and show that the central charge $c = 1$ in the SL phases. As a result, the central charge c is close to the exact value $c = 1$, with a relative error being less than 4%. These results show that both the SL_C and the SL_{IC} phases are the Luttinger liquids. To further confirm that, the Luttinger parameter K is also extracted according to the bipartite fluctuations in the SL phases (see Appendix B for details).

Note that the magnetization plateaus in the AFM, FM, and 10 phases correspond to the fidelity plateaus on the fidelity surface: all of these phases are, respectively, described in terms of a single ground-state wave function, independent of the control parameters. Therefore, these phases are gapped. As such, all phase transitions from Luttinger liquids to the AFM, FM, and 10 phases, which arise from level crossings

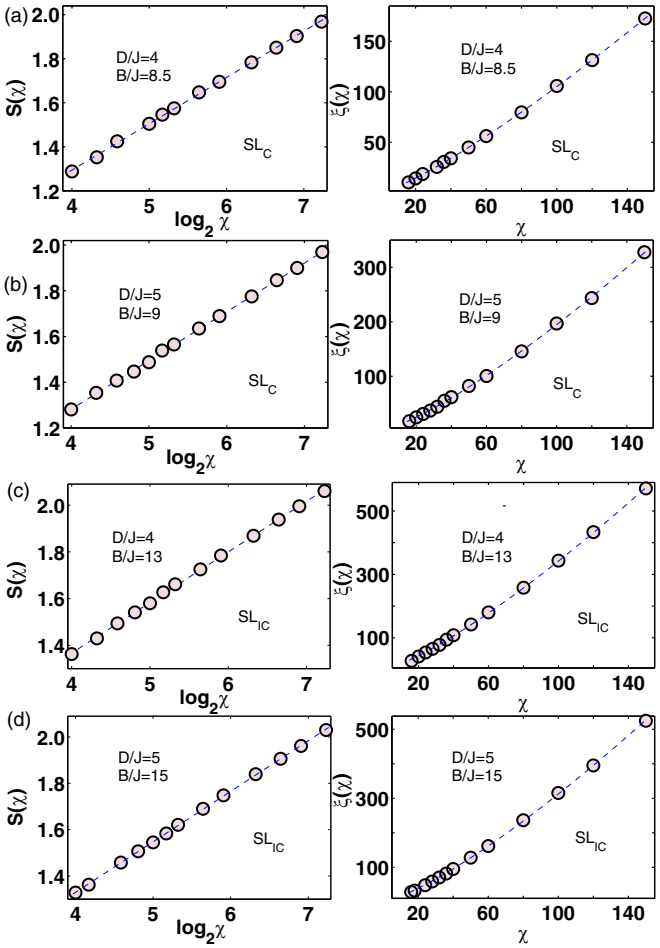

FIG. 3. The scaling of the von Neumann entropy S with respect to the bond dimension χ, $S(\chi) = \frac{c\kappa}{6} \log_2 \chi + b$, and the correlation length $\xi(\chi)$ as a function of the bond dimension χ, $\xi(\chi) = a\chi^{\kappa}$, for the SL_C phase [panels (a) and (b)] and the SL_{IC} phase [panels (c) and (d)].

due to conservation of the magnetization along the external magnetic field direction, belong to the PT universality class. This is also consistent with the continuity of the ground-state fidelity per site with respect to the control parameters D/J and B/J around all these phase transition points.

TABLE I. The finite-entanglement scaling exponents κ and central charges c for four chosen points deep inside the SL_C and SL_{IC} phases.

	SL_C $D/J=4$ $B/J=8.5$	SL_C $D/J=5$ $B/J=9$	SL_{IC} $D/J=4$ $B/J=13$	SL_{IC} $D/J=5$ $B/J=15$
κ	1.225(9)	1.28(2)	1.28(2)	1.29(1)
$c\kappa/6$	0.210(4)	0.213(3)	0.217(3)	0.218(2)
c	1.03(3)	1.00(3)	1.02(2)	1.02(2)

V. CHARACTERIZATION OF PHASES

Given that the ground-state phase diagram has seven different regions, the remaining task is to characterize their exact nature. To characterize the SS phase, the SL_C phase, the SL_{IC} phase, and the IC phase, we calculate the spin correlation functions $\langle S_i^z S_j^z \rangle$ and $\langle \mathbf{S}_i^+ \mathbf{S}_j^- \rangle$ and the mutual information $I(r)$, with $r = |i - j|$ being the lattice distance, respectively. A Fourier transform allows the spin structure factor to be written as [2]

$$S^{zz}(\mathbf{q}) = \sum_j e^{-i\mathbf{q}\cdot(r_0 - r_j)} \langle S_0^z S_j^z \rangle,$$
$$S^{+-}(\mathbf{q}) = \sum_j e^{-i\mathbf{q}\cdot(r_0 - r_j)} \langle \mathbf{S}_0^+ \mathbf{S}_j^- \rangle. \quad (6)$$

Mutual information is a standard measure of correlation between two random variables in classical information theory. Quantum mutual information can be defined [29–33] by replacing the Shannon entropy in the classical information theory with the von Neumann entropy, which can quantify the total correlation including classical and quantum correlations in a bipartite quantum state [30]. The quantum mutual information between sites A and B can be written as

$$I(A : B) = S_A + S_B - S_{AB}, \quad (7)$$

where $S = -\mathrm{Tr}\rho \ln \rho$ is the von Neumann entropy and ρ denotes the reduced density matrix.

A. AFM, FM, and 10 phases

Three of these phases (the AFM, FM, and 10 phases) admit a local-order parameter. A common prominent feature of these three phases is that they are seen as three fidelity plateaus on the fidelity surfaces, which correspond to the three magnetization plateaus in Fig. 4. Here, we assume that the single-ion anisotropy $D/J = 4$, the exchange anisotropy $\Delta = 6$, and the magnetic field strength B/J varies from 4 to 20, with the bond dimension $\chi = 60$. Note that, on each fidelity plateau, $d(B_1/J, B_2/J) = 1$ is satisfied, which implies that the system is described by a single ground-state wave function, independent of the control parameter B/J.

In order to characterize the AFM, FM, and 10 phases, here, we defined a magnetization $M_1^z = \langle (S_i^z + S_{i+1}^z)/2 \rangle$ and a staggered magnetization $M_2^z = \langle (S_i^z - S_{i+1}^z)/2 \rangle$. The magnetization M_1^z and the staggered magnetization M_2^z along the magnetic field direction shown in Fig. 4 also reflect differences between different phases: the AFM plateau with antiparallel spin alignment ($M_1^z = 0, M_2^z = 1$), the FM plateau with parallel spin alignment ($M_1^z = 1, M_2^z = 0$), and the half-magnetization plateau corresponding to the 10 phase ($M_1^z = 0.5$). The latter describes a macroscopic superposition state with two configurations: $(1010\cdots)$ and $(0101\cdots)$. That is, the fraction of spins "−1" in the AFM configuration are replaced by spins "0", such that the averaged value of the odd and even sites per site takes 0.5 rather than 1 or 0 at a single site. Except for the three magnetization plateaus, the magnetization M_1^z always increases with increasing external magnetic field strength B/J.

Here, we stress that the occurrence of the magnetization plateaus with $M_1^z = 0$, 0.5, and 1 is consistent with the

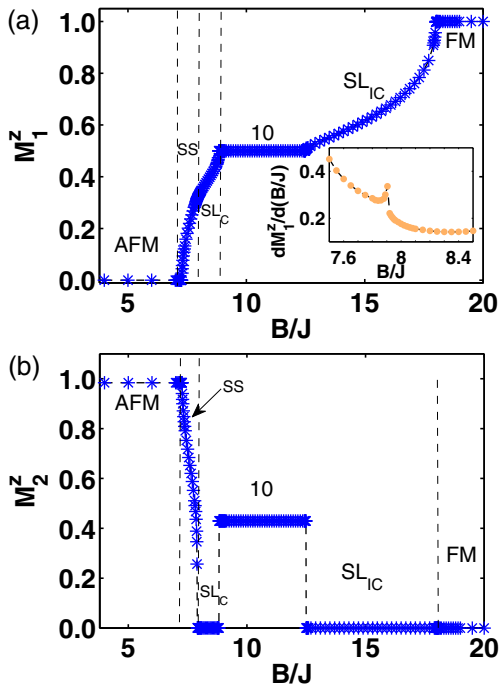

FIG. 4. (a) The magnetization M_1^z and (b) the staggered magnetization M_2^z, as a function of external magnetic field B/J for $\Delta = 6$ and $D/J = 4$, with the bond dimension $\chi = 60$. In the inset of panel (a), we show the first-order derivative of the magnetization M_1^z as a function of B/J, and a singularity point corresponds to the phase transition point between the SS and SL_C phases.

proposal that, in one dimension, the magnetization M_1^z at a plateau in the magnetization curve satisfies $SV(1 - M_1^z) \in \mathbf{Z}$, with $\mathbf{Z}$ denoting the set of integers, S being the size of a local spin, and V being the number of spins in a translational unit cell of a given ground-state wave function [22]. An intriguing fact is that a magnetization plateau corresponds to a fidelity plateau on the ground-state fidelity surface, thus offering an alternative route to investigate the magnetization processes of quantum many-body spin systems [34].

B. SS phase

Due to the competition between the exchange and single-ion anisotropies, an exotic SS phase occurs in a narrow region between the AFM and 10 phases. In the SS phase, $\langle S_i^z \rangle$ takes on different values at odd and even sites without uniformity, in sharp contrast with the SL phases. The average value is nonzero with the net magnetization, which is consistent with previous results [2,3] with an Ising-like order. As a detailed characterization of the SS phase, Fig. 5(a) plots (left panel) the longitudinal spin correlations $\langle S_i^z S_j^z \rangle$ and Fig. 5(b) plots (left panel) the transversal spin correlations $\langle \mathbf{S}_i^+ \mathbf{S}_j^- \rangle$, which take finite values even if the distance is as far as up to 500, for a typical ground state ($D/J = 3, B/J = 9$) in the SS phase, with the bond dimension $\chi = 200$. Specifically, in the longitudinal direction, we see that $S^{zz}(\pi)$ occurs as a peak and $S^{zz}(0)$ as a dip. The transversal correlation approaches saturation with an algebraic decay. The nonvanishing transversal and longitudinal spin correlations guarantee, even in the thermodynamic

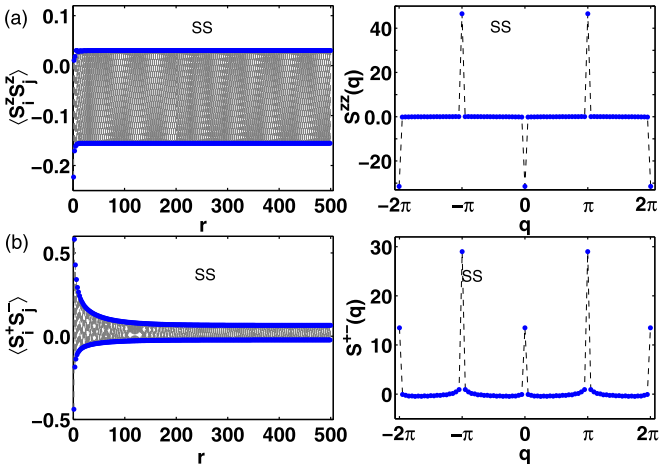

FIG. 5. In the SS phase with $D/J = 3$ and $B/J = 9$: (a) (left panel) the longitudinal correlation $\langle S_i^z S_j^z \rangle$ and (b) (left panel) the transversal correlation $\langle \mathbf{S}_i^+ \mathbf{S}_j^- \rangle$. The corresponding momentum distribution of the structure factor: (a) (right panel) $S^{zz}(q)$ and (b) (right panel) $S^{+-}(q)$, with the bond dimension $\chi = 200$.

limit, the coexistence of the diagonal and off-diagonal order. Note that the peaks for the transversal structure factor $S^{+-}(q)$ is located at a multiple of π.

Figure 6(a) plots the mutual information $I(r)$ as a function of the lattice distance $r = |i - j|$, for a typical ground state ($D/J = 3, B/J = 9$) in the SS phase, with the bond dimension $\chi = 200$. In the SS phase, the mutual information $I(r)$ shows a power-law decay at odd and even lattice distance r, respectively. In Fig. 6(b), the ln-ln plot shows clearly the mutual information $I(r)$ undergoes a power-law decay to zero as the lattice distance increases to the infinity. The power-law decaying part increases as the bond dimension increases. Here, we take the even lattice distance $r = 2|i - j|$ in Fig. 6(b). In order to confirm the power-law decay of the mutual information, we perform a numerical fit for the power-law decaying part with the fitting function $\ln I(r) = -\eta \ln r + d$. The exponents of the mutual information are given as $\eta = 1.34(2)$, $1.24(1)$, $1.18(1)$, and $1.16(1)$ for the bond dimensions $\chi = 50$, 100, 150, and 200, respectively. The result implies that the expo-

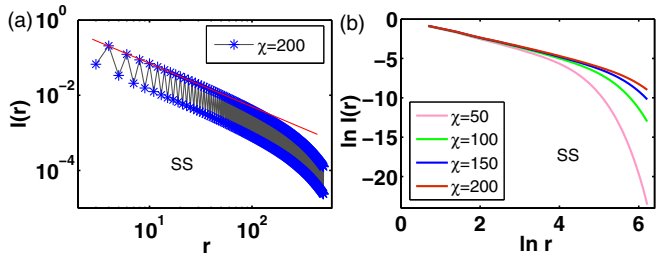

FIG. 6. (a) Mutual information $I(r)$ as a function of the lattice distance $r = |i - j|$ for a typical ground state in the SS phase with the bond dimension $\chi = 200$. (b) Mutual information $\ln I(r)$ as a function of the lattice distance $\ln r$ with the lattice distance $r = 2|i - j|$ for various bond dimensions χ. The exponent η of the mutual information is extracted for the power-law decaying part in panel (b) for the bond dimensions $\chi = 50$, 100, 150, and 200, respectively. Here, $D/J = 3$ and $B/J = 9$ for the SS phase.

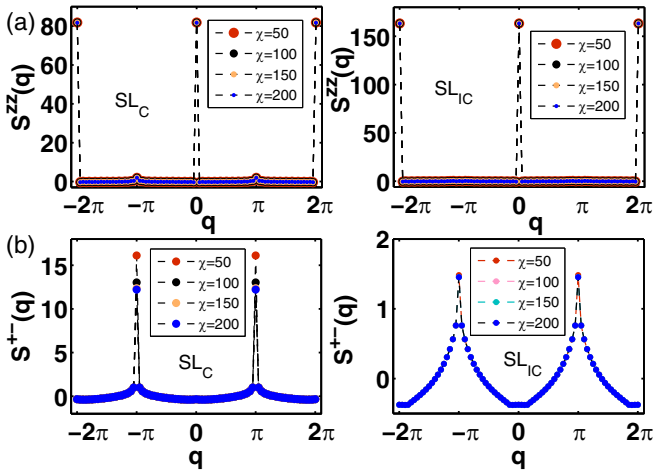

FIG. 7. Momentum distribution of the structure factors (a) $S^{zz}(q)$ and (b) $S^{+-}(q)$ for two typical ground states in the SL_C and SL_{IC} phases, respectively. Here, $D/J = 4$ and $B/J = 8.5$ for the SL_C phase, and $D/J = 5$ and $B/J = 15$ for the SL_{IC} phase. The different colors denote the simulation results from different bond dimensions.

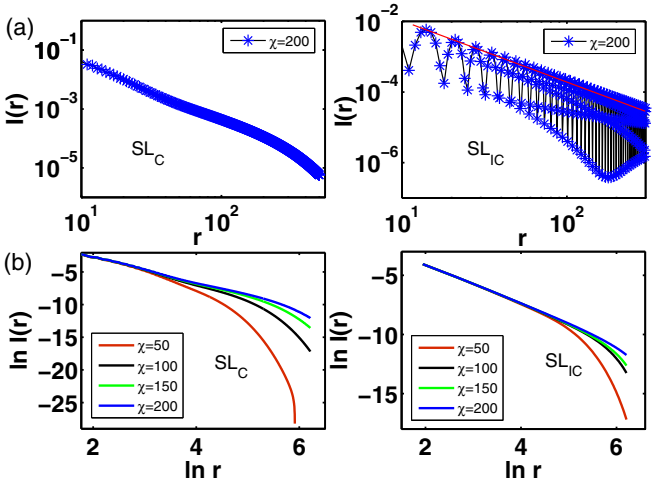

FIG. 8. (a) Mutual information $I(r)$ as a function of the lattice distance $r = |i - j|$ for two typical ground states in the SL_C and SL_{IC} phases with the bond dimension $\chi = 200$. (b) Mutual information $\ln I(r)$ as a function of the lattice distance $\ln r$ with the lattice distance $r = 7|i - j|$ for various bond dimensions χ. The exponent η of the mutual information can be extracted for the power-law decaying part in panel (b), for two typical ground states in the SL_C and SL_{IC} phases, respectively. Here, $D/J = 4$ and $B/J = 8.5$ for the SL_C phase, and $D/J = 5$ and $B/J = 15$ for the SL_{IC} phase.

nent of the power-law decay decreases as the bond dimension increases.

C. SL_C and SL_{IC} phases

Let us turn to the commensurate and incommensurate SL phases. Physically, "incommensurate" means the wavelength of the oscillation pattern is not an integer multiple of the lattice spacing. As aforesaid, the SS phase can be characterized by the nonvanishing transversal and longitudinal spin correlations. Following the SS phase, we calculate also the transversal and longitudinal spin correlations for the SL_C and SL_{IC} phases. Figure 7 plots the momentum distribution of structure factors (a) $S^{zz}(q)$ and (b) $S^{+-}(q)$ for two typical ground states in the SL_C phase ($D/J = 4$, $B/J = 8.5$) and the SL_{IC} phase ($D/J = 5$, $B/J = 15$), respectively. Here, the bond dimensions $\chi = 50$, 100, 150, and 200. From Fig. 7, we do not see a peak at some q between 0 and 2π except 0, $\pm\pi$, and $\pm 2\pi$ on $S^{zz}(q)$ and $S^{+-}(q)$ in the SL_{IC} phase. The spin-liquid phase is characterized by long-range quantum entanglement and without long-range order. Therefore, the oscillation pattern of the SL_{IC} phase should be seen in the entanglement measure, not in spin correlation.

In order to distinguish clearly the SL_C and SL_{IC} phases, we calculate the mutual information in Fig. 8. From Fig. 8(a), we see a remarkable difference in the mutual information between two typical ground states in the SL_C and SL_{IC} phases with the bond dimension $\chi = 200$: for a sufficiently large lattice distance r, the mutual information $I(r)$ shows almost a monotonic power-law decay as the lattice distance $r = |i - j|$ increases in the SL_C phase and the dominant decaying term of the mutual information $I(r)$ is proportional to $r^{-\eta}$. Here, the exponents $\eta = 2.2(2)$, 2.18(7), 2.13(4), and 2.07(4) are extracted from the fitting function $\ln I(r) = -\eta \ln r + d$ for the power-law decaying part in Fig. 8(b) (left panel) for a typical ground state ($D/J = 4$, $B/J = 8.5$) in the SL_C phase with the bond dimensions $\chi = 50$, 100, 150, and 200, respectively. It is close to 2 as the bond dimension increases. Moreover, for a sufficiently large lattice distance $r = |i - j|$, the dominant decaying term of the mutual information $I(r)$ is expected to be proportional to $r^{-\eta}\cos(qr)$ in the SL_{IC} phase in Fig. 8(a) (right panel). Here, $q = \alpha\pi(1 - m^z)$ [6], with α being the fitting constant and m^z being the magnetization per site along the z direction. Next, such a behavior will be confirmed for a typical ground state ($D/J = 5$, $B/J = 15$) in the SL_{IC} phase. Note that the data in Fig. 8(b) (right panel) come from the decaying term $r^{-\eta}$ of the mutual information $I(r)$ with the lattice distance $r = 7|i - j|$. Here, the exponents $\eta = 1.69(3)$, 1.67(1), 1.66(1), and 1.66(1) are extracted from the fitting function $\ln I(r) = -\eta \ln r + d$ for the power-law decaying part in Fig. 8(b) (right panel) with the bond dimensions $\chi = 50$, 100, 150, and 200, respectively. The result implies that the exponent of the power-law decay tends to a finite value as the bond dimension increases.

As an illustrative example, we choose one site deep inside the SL_{IC} phase. Figure 9 plots the mutual information $I(r)$ as a function of the lattice distance $r = |i - j|$ with the bond dimension $\chi = 200$ for $D/J = 5$ and $B/J = 15$ in the SL_{IC} phase. Here, the red dots denote the data and the solid black line is the fitted line. To confirm the decaying form of the mutual information $I(r)$, we performed a numerical fit with the fitting function $I(r) = er^{-\eta}\cos(qr) + fr^{-1} + g$, with $q = \alpha\pi(1 - m^z)$. Here, e, f, g, and α are fitting constants. The fitting constants are given as $e = 0.312$, $f = 0.031\,55$, $g = -0.000\,16$, and $\alpha = 0.6704$ with the exponent $\eta = 1.657$ and the magnetization $m^z = 0.572$. For a sufficiently large lattice distance r, our result indicates that the dominant decaying term of the mutual information $I(r)$ is proportional to $r^{-\eta}\cos(qr)$, with $q = \alpha\pi(1 - m^z)$, in the SL_{IC} phase.

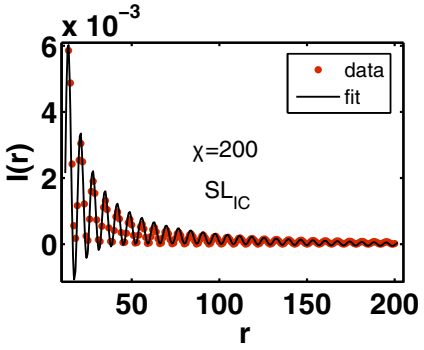

FIG. 9. The mutual information $I(r)$ as a function of the lattice distance r with the bond dimension $\chi = 200$ for $D/J = 5$ and $B/J = 15$ in the SL_{IC} phase. The black line is the numerical fitting function $I(r) = er^{-\eta}\cos(qr) + fr^{-1} + g$, with $q = \alpha\pi(1 - m^z)$. Here, e, f, g, and α are fitting constants.

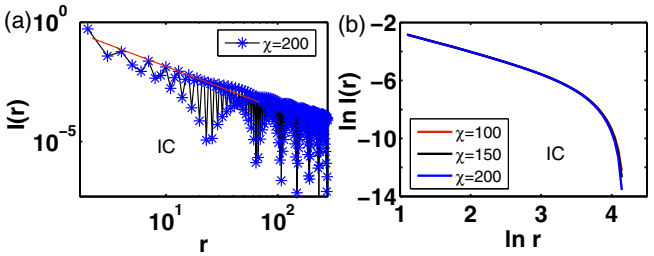

FIG. 11. (a) Mutual information $I(r)$ as a function of the lattice distance r with $r = |i - j|$ for the bond dimension $\chi = 200$. (b) Mutual information $\ln I(r)$ as a function of the lattice distance $\ln r$ with the lattice distance $r = 3|i - j|$ for various bond dimensions χ. The exponent η of mutual information can be extracted for the power-law decaying part in panel (b) for the bond dimensions $\chi = 50$, 100, 150, and 200, respectively. Here, $D/J = -3$ and $B/J = 12$ for the IC phase.

D. IC phase

As for the IC phase, Fig. 10(a) shows the longitudinal structure factor $S^{zz}(q)$, which is peaked at $q = 0$ and $\pm 2\pi$, indicating the appearance of the ferromagnetic order, although the off-diagonal order vanishes in the thermodynamic limit. In addition, we can see some small peaks around $q = \pm 0.65\pi$ and $\pm 1.35\pi$ in the inset of Fig. 10(a); this indicates that the IC phase has an incommensurate oscillation pattern in the longitudinal spin correlations. Figure 10(b) shows the transversal structure factor $S^{+-}(q)$, which is peaked at $\pm\pi$. Figure 11(a) shows the mutual information $I(r)$, and similar to the SL_{IC} phase, the dominant decaying term of the mutual information $I(r)$ is proportional to $r^{-\eta}\cos(qr)$. Next, such a behavior will be confirmed for a typical ground state ($D/J = -3, B/J = 12$) in the IC phase. Note that the data in Fig. 11(b) come from the decaying term $r^{-\eta}$ of the mutual information $I(r)$ with the lattice distance $r = 3|i - j|$. Here, the exponents $\eta = 1.4(1)$, 1.4(1), and 1.4(1) are extracted from the fitting function $\ln I(r) = -\eta \ln r + d$ for the power-law decaying part in Fig. 11(b) with the bond dimensions $\chi = 100$, 150, and 200, respectively. The result implies that different bond dimensions provide qualitatively consistent results.

In the IC phase, we also plot the mutual information $I(r)$ as a function of the lattice distance $r = |i - j|$ with the bond dimension $\chi = 200$ for $D/J = -3$ and $B/J = 12$ in Fig. 12. By using the same fitting function, i.e., $I(r) = er^{-\eta}\cos(qr) + fr^{-1} + g$, with $q = \alpha\pi(1 - m^z)$, the fitting constants are given as $e = 0.1808$, $f = 0.0489$, $g = -0.000\,19$, and $\alpha = 1.001(5)$ with the exponent $\eta = 1.359$ and the magnetization $m^z = 0.341$. Similar to the SL_{IC} phase, for a sufficiently large lattice distance r, the dominant decaying term of $I(r)$ is proportional to $r^{-\eta}\cos(qr)$ in the IC phase.

As a result, the mutual information $I(r)$ exhibits different decay behaviors in commensurate and incommensurate phases, respectively. Our results show that the dominant decaying term of the mutual information $I(r)$ is proportional to $r^{-\eta}$ in the commensurate phase and is proportional to $r^{-\eta}\cos(qr)$, with $q = \alpha\pi(1 - m^z)$, in the incommensurate phase.

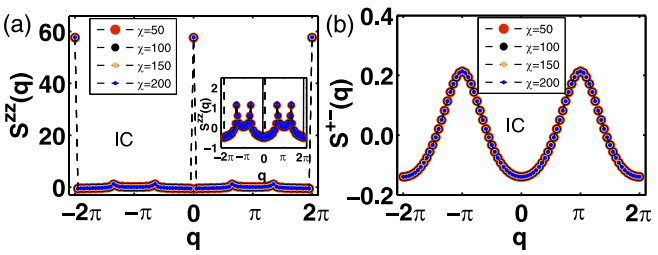

FIG. 10. Momentum distribution of the structure factors (a) $S^{zz}(q)$ and (b) $S^{+-}(q)$ for various bond dimensions χ. Here, $D/J = -3$ and $B/J = 12$ in the IC phase. The inset shows a magnification of the $S^{zz}(q)$.

VI. CONCLUSIONS

The spin-one quantum Heisenberg antiferromagnetic chain with exchange and single-ion anisotropies in an external magnetic field is investigated by using the iTEBD method. The ground-state phase diagram is identified *solely* by computing the ground-state fidelity per lattice site. Three fidelity plateaus appear on the fidelity surface, corresponding to the AFM, 10, and FM phases. Our results indicate that a magnetization

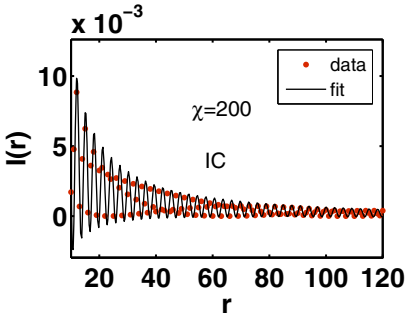

FIG. 12. The mutual information $I(r)$ as a function of the lattice distance r with the bond dimension $\chi = 200$ for $D/J = -3$ and $B/J = 12$ in the IC phase. The black line is the numerical fitting function $I(r) = er^{-\eta}\cos(qr) + fr^{-1} + g$, with $q = \alpha\pi(1 - m^z)$. Here, e, f, g, and α are fitting constants.

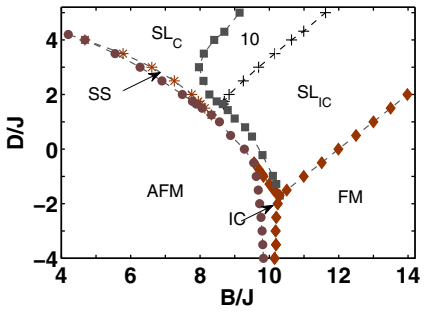

FIG. 13. : The ground-state fidelity phase diagram for the spin-1 anisotropic Heisenberg chain in the $(D/J, B/J)$ plane with $\Delta = 5$. Here, we have assumed J to be equal to 1 as the energy scale. The dashed lines are just a guide for the eyes.

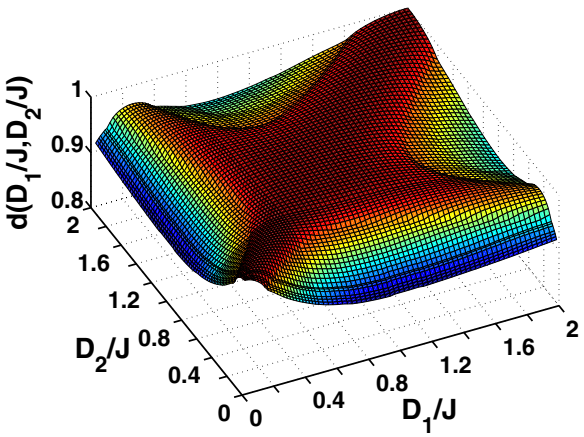

FIG. 14. The ground-state fidelity surface defined by the ground-state fidelity per site $d(D_1/J, D_2/J)$ as a function of D_1/J and D_2/J, two different values of the external magnetic field strength D/J. Here, the External field is fixed as $B/J = 9.3$.

plateau corresponds to a fidelity plateau on the ground-state fidelity surface. This offers an alternative route to investigate the magnetization processes of quantum many-body spin systems.

In addition, we perform a finite-entanglement scaling analysis of the von Neumann entropy and the correlation length with respect to the bond dimension, thus determining the central charge $c = 1$ in the SL phase and affirming that all transitions from the spin liquids to the magnetization plateaus belong to the PT universality class. Finally, we characterize all relevant phases that exhibit distinguishable magnetization processes with an increasing external magnetic field. The spin correlations, structure factors, and mutual information clearly characterize their dominant magnetic behavior. We confirm the coexistence of the diagonal order and the off-diagonal order in the SS phase, demonstrate the difference between the SL_C and SL_{IC} phases, and unveil the characteristics of the IC phase.

ACKNOWLEDGMENTS

The work is supported by the National Natural Science Foundation of China (Grant No. 11805285), the Science and Technology Research Program of the Chongqing Municipal Education Commission (Grants No. KJQN 201900703 and No. KJZD-K202103401), the Natural Science Foundation of Chongqing of China (Grant No. cstc2020jcyj-msxmX0034), and the Natural Science Foundation of Shaanxi Province of China (Grant No. 2022JM-033). We thank Qian-Qian Shi, Li-Ping Yang, and Bo Li for enlightening discussions.

APPENDIX A: GROUND-STATE FIDELITY PHASE DIAGRAM FOR EXCHANGE ANISOTROPY $\Delta = 5$

We investigate the ground-state phase diagram for the model (1) with exchange anisotropy $\Delta = 5$ by computing the ground-state fidelity per lattice site [13]. The ground-state fidelity per lattice site enables us to determine the ground-state phase diagram with no prior knowledge of the order parameters. Figure 13 plots the ground-state fidelity phase diagram in the $(D/J, B/J)$ plane. It consists of the conventional AFM and FM phases, an exotic SS phase, the SL_C phase, and the SL_{IC} phase, as well as the 10 phase and the IC phase. The overall phase landscape identified from the ground-state fidelity surfaces is in good agreement with the previous results from the DMRG calculations [5,7].

Note that the phase transition between the commensurate and incommensurate SL corresponds to a pinch point on the ground-state fidelity surface, as shown in Fig. 14, where the ground-state fidelity per lattice site $d(D_1/J, D_2/J)$ is plotted as a function of D_1/J and D_2/J for a typical choice of the control parameters: the exchange anisotropy $\Delta = 5$ and the external field $B/J = 9.3$, but the single-ion anisotropy D/J varies from 0 to 2. The singularity appearing on the fidelity surface is relatively weak. Nevertheless, we are still able to discern the pinch point, thus locating the phase transition point.

APPENDIX B: THE BIPARTITE FLUCTUATIONS

In addition, to identify both the commensurate and the incommensurate SL phases as Luttinger liquids, we apply a scaling analysis for the bipartite fluctuations. The bipartite fluctuations can be defined as [35,36]

$$\mathcal{F}(\chi) = \sum_{i,j} \left[\langle S_i^z S_j^z\rangle - \langle S_i^z\rangle\langle S_j^z\rangle\right], \tag{B1}$$

which satisfies [35–37]

$$\mathcal{F}(\chi) = \frac{K}{2\pi^2} \ln \xi(\chi) + \text{const.}, \tag{B2}$$

allowing us to extract the Luttinger parameter K. According to the U(1) quantum number (i.e., either the particle number n or the spin projection S_z) [35,38], the bipartite fluctuations

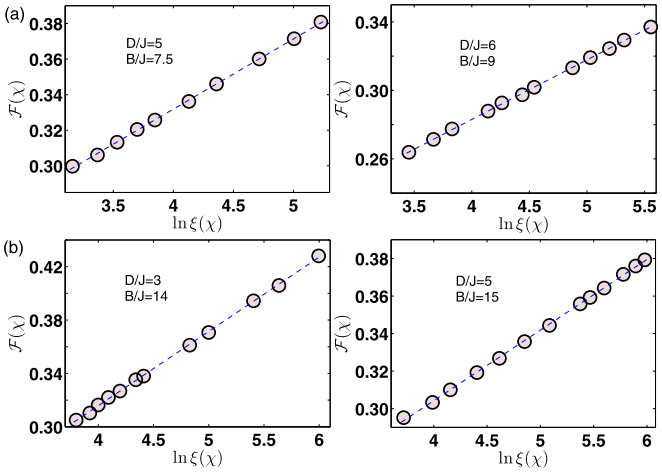

FIG. 15. The finite-entanglement scaling: bipartite fluctuations $\mathcal{F}(\chi)$ versus $\ln\xi(\chi)$. The bond dimension χ ranges from 24 to 120. Here, $D/J = 5$, $B/J = 7.5$ and $D/J = 6$, $B/J = 9$ for the SL_C phase and $D/J = 3$, $B/J = 14$ and $D/J = 5$, $B/J = 15$ for the SL_{IC} phase.

can be written in the Schmidt basis as

$$\mathcal{F} = \sum_x x^2 \sum_i \left(\lambda_i^x\right)^2 - \left[\sum_x x \sum_i \left(\lambda_i^x\right)^2\right]^2, \qquad \text{(B3)}$$

where x is the quantum number and λ_i is the Schmidt decomposition coefficient. Note that the sum $\sum_i$ is restricted to a fixed value of the quantum number x.

Figure 15 plots the bipartite fluctuations $\mathcal{F}(\chi)$ versus $\ln\xi(\chi)$, with the bond dimension χ ranging from 24 to 120, for four chosen points deep inside the SL_C and SL_{IC} phases. The best linear fit is exploited to estimate the Luttinger parameter K, which is listed in Table II. It shows that the Luttinger parameter K varies with the parameters D/J and B/J.

TABLE II. The Luttinger parameter K is extracted for four chosen points deep inside the SL_C and SL_{IC} phases. Here, the bond dimension χ ranges from 24 to 120.

	SL_C $D/J = 5$ $B/J = 7.5$	SL_C $D/J = 6$ $B/J = 9$	SL_{IC} $D/J = 3$ $B/J = 14$	SL_{IC} $D/J = 5$ $B/J = 15$
K	0.78(1)	0.687(8)	1.10(2)	0.74(1)

[1] D. Rossini, V. Giovannetti, and R. Fazio, Phys. Rev. B **83**, 140411(R) (2011).
[2] P. Sengupta and C. D. Batista, Phys. Rev. Lett. **98**, 227201 (2007).
[3] P. Sengupta and C. D. Batista, Phys. Rev. Lett. **99**, 217205 (2007).
[4] D. Peters, I. P. McCulloch, and W. Selke, Phys. Rev. B **79**, 132406 (2009).
[5] D. Peters, I. P. McCulloch, and W. Selke, J. Phys.: Conf. Ser. **200**, 022046 (2010).
[6] D. Peters, I. P. McCulloch, and W. Selke, Phys. Rev. B **85**, 054423 (2012).
[7] W. Selke, G. Bannasch, M. Holtschneider, I. P. McCulloch, D. Peters, and S. Wessel, Condens. Matter Phys. **12**, 547 (2009).
[8] R. T. S. Freire and J. A. Plascak, Phys. Rev. E **91**, 032146 (2015)
[9] Ü. Akıncı, J. Magn. Magn. Mater. **397**, 247 (2016).
[10] E. Kim and M. H. N. Chan, Nature (London) **427**, 225 (2004).
[11] V. L. Pokrovsky and A. L. Talapov, Phys. Rev. Lett. **42**, 65 (1979).
[12] H.-Q. Zhou and J. P. Barjaktarevič, J. Phys. A: Math. Theor. **41**, 412001 (2008); H.-Q. Zhou, J.-H. Zhao, and B. Li, *ibid.* **41**, 492002 (2008).
[13] H.-Q. Zhou, R. Orús, and G. Vidal, Phys. Rev. Lett. **100**, 080601 (2008).
[14] J.-H. Zhao and H.-Q. Zhou, Phys. Rev. B **80**, 014403 (2009).
[15] J.-H. Zhao, H.-L. Wang, B. Li, and H.-Q. Zhou, Phys. Rev. E **82**, 061127 (2010).
[16] H.-L. Wang, A.-M. Chen, B. Li, and H.-Q. Zhou, J. Phys. A: Math. Theor. **45**, 015306 (2012); Y.-W. Dai, B.-Q. Hu, J.-H. Zhao, and H.-Q. Zhou, *ibid.* **43**, 372001 (2010); Y.-W. Dai, S. Y. Cho, M. T. Batchelor, and H.-Q. Zhou, Phys. Rev. E **89**, 062142 (2014).
[17] S.-H. Li, Q.-Q. Shi, M. T. Batchelor, and H.-Q. Zhou, New J. Phys. **19**, 113027 (2017); Y.-W. Dai, Q.-Q. Shi, S. Y. Cho, M. T. Batchelor, and H.-Q. Zhou, Phys. Rev. B **95**, 214409 (2017).
[18] S. Sachdev, *Quantum Phase Transitions* (Cambridge University, Cambridge, England, 1999).
[19] X.-G. Wen, *Quantum Field Theory of Many-Body Systems* (Oxford University, Oxford, 2004).
[20] G. Vidal, Phys. Rev. Lett. **98**, 070201 (2007).
[21] T. Tonegawa, K. Okunishi, T. Sakai, and M. Kaburagi, Prog. Theor. Phys. Suppl. **159**, 77 (2005).
[22] M. Oshikawa, M. Yamanaka, and I. Affleck, Phys. Rev. Lett. **78**, 1984 (1997).
[23] L. Amico, R. Fazio, A. Osterloh, and V. Vedral, Rev. Mod. Phys. **80**, 517 (2008).
[24] P. Calabrese and J. Cardy, J. Stat. Mech.: Theory Exp. (2004) P06002.
[25] L. Tagliacozzo, T. R. de Oliveira, S. Iblisdir, and J. I. Latorre, Phys. Rev. B **78**, 024410 (2008).
[26] F. Pollmann, S. Mukerjee, A. M. Turner, and J. E. Moore, Phys. Rev. Lett. **102**, 255701 (2009).
[27] G. Vidal, J. I. Latorre, E. Rico, and A. Kitaev, Phys. Rev. Lett. **90**, 227902 (2003); V. E. Korepin, *ibid.* **92**, 096402 (2004).
[28] J.-H. Liu, Q.-Q. Shi, H.-L. Wang, J. Links, and H.-Q. Zhou, Phys. Rev. E **86**, 020102(R) (2012).
[29] Y.-W. Dai, X.-H. Chen, S. Y. Cho, H.-Q. Zhou, and D.-X. Yao, arXiv:1805.03464.
[30] B. Groisman, S. Popescu, and A. Winter, Phys. Rev. A **72**, 032317 (2005).

[31] C. Adami and N. J. Cerf, Phys. Rev. A **56**, 3470 (1997).
[32] F. C. Alcaraz and M. A. Rajabpour, Phys. Rev. B **91**, 155122 (2015).
[33] B. Schumacher and M. D. Westmoreland, Phys. Rev. A **74**, 042305 (2006).
[34] A. Honecker, J. Schulenburg, and J. Richter, J. Phys.: Condens. Matter **16**, S749 (2004).
[35] H. F. Song, S. Rachel, and K. Le Hur, Phys. Rev. B **82**, 012405 (2010).
[36] H. F. Song, S. Rachel, C. Flindt, I. Klich, N. Laflorencie, and K. Le Hur, Phys. Rev. B **85**, 035409 (2012).
[37] J. A. Kjäll, M. P. Zaletel, R. S. K. Mong, J. H. Bardarson, and F. Pollmann, Phys. Rev. B **87**, 235106 (2013).
[38] U. Schollwöck, Rev. Mod. Phys. **77**, 259 (2005).